Liodakis, I.; Hovatta, T.; Aller, M. F.; Aller, H. D.; Gurwell, M. A.; Lähteenmäki, A.; Tornikoski, M.

Identifying changing jets through their radio variability

Astronomy & Astrophysics

Identifying changing jets through their radio variability

I. Liodakis[1], T. Hovatta[1,2], M. F. Aller[3], H. D. Aller[3], M. A. Gurwell[4], A. Lähteenmäki[2,5], and M. Tornikoski[2]

[1] Finnish Center for Astronomy with ESO, University of Turku, Quantum, Vesilinnantie 5, 20014 Turku, Finland
  e-mail: `yannis.liodakis@utu.fi`
[2] Aalto University Metsähovi Radio Observatory, Metsähovintie 114, 02540 Kylmälä, Finland
[3] Department of Astronomy, University of Michigan, Ann Arbor, MI 48109-1107, USA
[4] Center for Astrophysics | Harvard & Smithsonian, 60 Garden Street, Cambridge, MA 02138, USA
[5] Aalto University Department of Electronics and Nanoengineering, PO Box 15500, 00076 Aalto, Finland

ABSTRACT

Context. Supermassive black holes can launch highly relativistic jets with velocities reaching Lorentz factors of as high as $\Gamma > 50$. How the jets accelerate to such high velocities and where along the jet they reach terminal velocity are open questions that are tightly linked to their structure as well as their launching and dissipation mechanisms.
Aims. Changes in the beaming factor along the jets could potentially reveal jet acceleration, deceleration, or bending. We aim to (1) quantify the relativistic effects in multiple radio frequencies and (2) study possible jet velocity–viewing angle variations at parsec scales.
Methods. We used the state-of-the-art code *Magnetron* to model light curves from the University of Michigan Radio Observatory and the Metsähovi Radio Observatory's monitoring programs in five frequencies covering about 25 years of observations in the 4.8 to 37 GHz range for 61 sources. We supplement our data set with high-frequency radio observations in the 100–340 GHz range from ALMA, CARMA, and SMA. For each frequency we estimate the Doppler factor which we use to quantify possible changes in the relativistic effects along the jets.
Results. The majority of our sources do not show any statistically significant difference in their Doppler factor across frequencies. This is consistent with constant velocity in a conical jet structure, as expected at parsec scales. However, our analysis reveals 17 sources where relativistic beaming changes as a function of frequency. In the majority of cases, the Doppler factor increases towards lower frequencies. Only 1253–053 shows the opposite behavior. By exploring their jet properties we find that the jet of 0420–014 is likely bent across the 4.8–340 GHz range. For 0212+735, the jet is likely parabolic, and still accelerating in the 4.8–37 GHz range. We discuss possible interpretations for the trends found in the remaining sources.

Key words. relativistic processes – galaxies: jets – galaxies: active

1. Introduction

Blazars are a subclass of active galactic nuclei (AGN) with powerful and energetic jets pointed towards our line of sight (Blandford et al. 2019). Due to the alignment of their jets, blazars are among the brightest and most variable sources from low-frequency radio all the way to very high-energy γ-rays. Their jets show complex structures from the smallest (e.g., Kim et al. 2020) to the largest scales (e.g., Kharb et al. 2010), with radio emission being an ever present piece of the relativistic jet puzzle. Understanding radio variability on diverse scales can therefore be a potential probe of many aspects of jet microphysics. It is therefore not surprising that several attempts have been made to understand the variability properties of blazars in the radio regime from different perspectives; for example, spectral and multiwavelength variability, variability amplitudes, beaming effects, and so on (e.g., Angelakis et al. 2010; Richards et al. 2014; Liodakis et al. 2017c, 2018).

Jets in blazars are highly relativistic with Lorentz factors (Γ) from a few to a few tens (e.g., Hovatta et al. 2009; Liodakis & Pavlidou 2015a; Liodakis et al. 2017b; Jorstad et al. 2017). Whether the jets are launched with such high Γ or are accelerated to the velocities measured at parsec scales is still an open question. Most likely the jets are highly magnetized when

launched and are accelerated through the conversion of magnetic to kinetic energy (Vlahakis & Königl 2004; Vlahakis 2004; Komissarov et al. 2007; Zhang & Giannios 2021). The jet is confined by either magnetic hoop stress (e.g., Spruit et al. 1997) or the pressure of the external medium (Lyubarsky 2009, 2010; Liodakis 2018) into a parabolic shape which favors acceleration. Acceleration continues until the jet magnetization parameter (σ_m), that is, the ratio of the magnetic to the kinetic energy flux, becomes $\sigma_m \leq 1$ when it likely stops (Vlahakis & Königl 2003, 2004; Lyubarsky 2009; Nokhrina et al. 2020). Contrary to observations, which are typically taken in flaring states, relativistic magnetohydrodynamic (RMHD) simulations typically yield Γ of only a few (e.g., Chatterjee et al. 2019). Very long baseline interferometry (VLBI) observations show that the jet in M87 has a parabolic shape up to the HST-1 region (e.g., Biretta et al. 1999) and then transitions to conical (Asada & Nakamura 2012). Recent observations of other nearby radio galaxies have found similar geometries suggesting this is a common feature of AGN jets (Kovalev et al. 2020; Boccardi et al. 2021), while theoretical works predict differences in the location of the transition region between blazar subclasses (Potter & Cotter 2015). Based on our current understanding of blazar jets (e.g., Blandford & Königl 1979; Marscher 1995; Marscher et al. 2008), gigahertz radio emission should arise at parsec scales where the jets are likely

conical and nonaccelerating. However, accelerating jet components found by the MOJAVE program at 15 GHz challenge this interpretation (Homan et al. 2009, 2015). Moreover, the "Doppler crisis", that is, the discrepancy between Doppler factors measured in the radio bands and that required to explain the high-energy emission in high-synchrotron peaked sources, has been interpreted either as the result of decelerating (e.g., Georganopoulos & Kazanas 2003) or structured jets (e.g., Piner & Edwards 2018). The Doppler factor (δ) is a function of the velocity and the viewing angle of the jet, defined as $\delta = 1/(\Gamma[1 - \beta\cos\theta])$, where θ is the viewing angle, $\beta = u/c$, where c is the speed of light, and $\Gamma = 1/\sqrt{(1 - \beta^2)}$.

To shed more light on the beaming profiles of the jets, we model the flux-density variations in multiple radio frequencies. Because of synchrotron self-absorption, the emission at different frequencies probes different locations along the jets. Hence, quantifying the relativistic effects as a function of frequency can help us to identify changes in the jet velocity or orientation at parsec scales. As flux-density variations occur predominately in the radio cores (Savolainen et al. 2002), this allows us to study sources where their jet structure is unresolved through VLBI. In Sect. 2 we discuss the sample and the tools used for the analysis of the radio light curves. In Sect. 3 we explore the relativistic effects as a function of frequency, and in Sect. 4 we explore the possible origin of the relativistic beaming variations and discuss our results. Our conclusions are presented in Sect. 5. Through the paper we have adopted a Λ CDM cosmological model with $\Omega_m = 0.27$, $\Omega_\Lambda = 1 - \Omega_m$ and $H_0 = 71$ km s^{-1} Mpc^{-1} (Komatsu et al. 2009).

2. Data and light-curve modeling

We use data from the Metsähovi and University of Michigan (UMRAO) Radio observatories for five frequencies: 4.8, 8, 14.5, 22, and 37 GHz covering a few decades of observations (Aller et al. 1985, 1999, 2014; Salonen et al. 1987; Teräsranta et al. 1992, 1998, 2004, 2005)[1]. Our sample consists of 61 common sources, 35 of which are flat-spectrum radio quasars (FSRQs), 22 are BL Lac objects (BL Lacs), 3 are radio galaxies, and one is unidentified. Our earliest observations start in 1965 at 8 GHz and the latest end in 2018 at 14.5 and 37 GHz. The light curves were analyzed using *Magnetron*[2]. Here we provide a brief description; more details can be found in Huppenkothen et al. (2015), and Liodakis et al. (2018).

Magnetron decomposes the light curves into a series of flares superimposed on a Ornstein–Uhlenbeck-type stochastic background. Each flare has decoupled exponential rise and exponential decay profiles fully described by four free parameters: position, rise time, amplitude, and flare skewness (decay time/rise time ratio). The parameter space is efficiently explored through diffusive nested sampling (Brewer et al. 2009; Brewer & Foreman-Mackey 2016). *Magnetron* does not deliver a best-fit solution for each source, but rather a posterior distribution of ~10^2 models of flares and backgrounds. These models represent the different realizations of the flaring activity and underlying stochastic variability in a source given the overall uncertainty in the flare parameters and flare blending, which becomes even more severe at the lower centimeter-band wavelengths. The number of flares is also a free parameter that can vary for different frequencies as shown in Fig. 1. Panels a–d show one randomly selected realization

of the flares in each frequency for 1633+382 (also know as 4C 38.41). Purely stochastic models using a single or a combination of multiple OU-processes have been used on γ-ray light curves (e.g., Sobolewska et al. 2014; Burd et al. 2021). However, there is strong evidence that multiwavelength flares, and especially radio flares, are connected to the ejection of jet components (e.g., Savolainen et al. 2002; Marscher et al. 2008; Liodakis et al. 2020) suggesting that a combination of flares and stochastic variability, such as the one used by *Magnetron*, is a more appropriate model.

For every frequency and for each source, we use the posterior distribution of flares to estimate the distribution of the highest brightness temperature from which we estimate the median and confidence intervals. During the fitting, we use all the available observations for a given source. However, the time period during which a source was observed by the Metsähovi and University of Michigan Radio observatories varies not only for each source but also for each frequency. Hence, it is possible for the light curves of one observatory to include flares not observed by the other. This can introduce a bias when looking for variations of the Doppler factor across frequencies. Therefore, in our analysis we only consider flares during the common observing periods between the observatories. The earliest flare we consider is at MJD 44401 (June 1980) while the latest is at MJD 53179 (June 2004). The variability brightness temperature is estimated as

$$T_{\text{var}} = 1.47 \cdot 10^{13} \frac{d_L^2 \Delta S_{\text{ob}}(\nu)}{\nu^2 t_{\text{var}}^2 (1 + z)^4} \, K, \tag{1}$$

where d_L is the luminosity distance (Mpc), $\Delta S_{\text{ob}}(\nu)$ the flare amplitude (Jy), ν the observing frequency (GHz), t_{var} the flare rise time (days), and z is the redshift. We find a wide range of observed brightness temperatures across frequencies. The values range from 10^8–10^9 K all the way to ~10^{16} K, with the median for each frequency being about 10^{13}–10^{14} K. We estimate the Doppler factor by marginalizing over the observed T_{var} distribution and the Gaussian model for the maximum intrinsic brightness temperature ($T_{\text{int,max}}$) found in Liodakis et al. (2018) with mean $\mu = 2.78 \times 10^{11}$ K and $\sigma = 0.72 \times 10^{11}$ using

$$\delta_{\text{var}} = (1 + z) \sqrt[3]{\frac{T_{\text{var}}}{T_{\text{int,max}}}}. \tag{2}$$

This process gives us a distribution of Doppler factors for each source from which we quote the median and 68% confidence intervals in Table A.1. An example of the posterior δ_{var} distribution in all frequencies for 0716+714 is shown in Fig. 2 (top panel). The range of Doppler factors is also wide, starting below unity for some radio galaxies, up to almost 60. The median value across frequencies is ~10 (Fig. 2 bottom panel).

3. Doppler factor versus frequency

Figure 1f shows an example of the Doppler factor versus frequency in log–log space for 1633+382. The resulting posterior distributions for the Doppler factor in individual sources are often asymmetric as shown in Fig. 2 (0716+714, top panel). We take that asymmetry into account when trying to statistically establish a persistent Doppler factor versus frequency trend for each source by randomly sampling the posterior δ_{var} distribution for each frequency. We create a new Doppler factor

---

[1] https://dept.astro.lsa.umich.edu/datasets/umrao.php
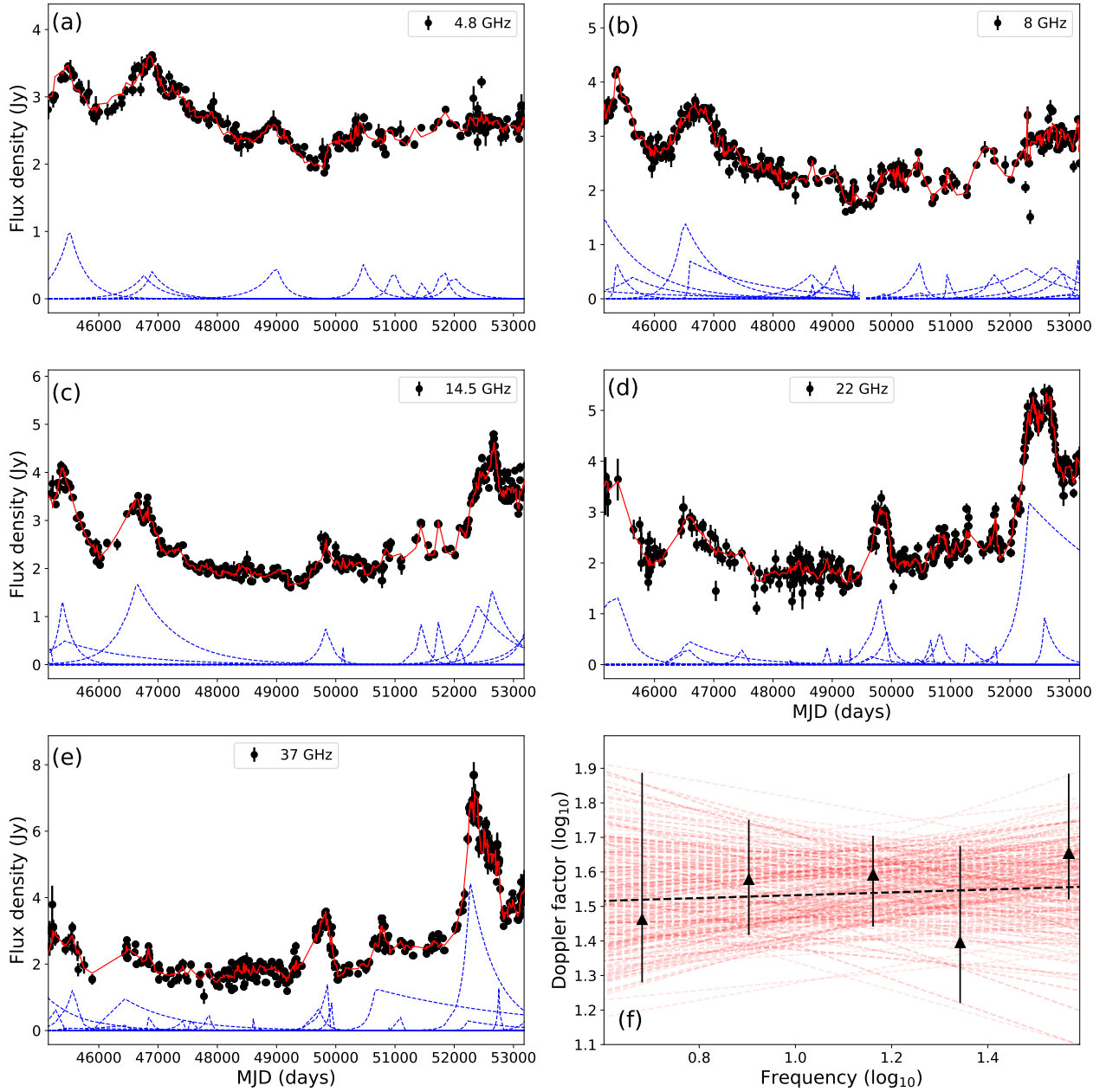[2] https://github.com/dhuppenkothen/magnetronhierarchy

Fig. 1. Example of light-curve fitting for 1633+382 for all frequencies (*panels a–e*). The red solid line shows the overall fit in each panel, whereas the blue lines show one randomly selected realization of the flares after subtraction of the background. Here we only consider flares from June 1982 to June 2004. *Panel f*: Doppler factor versus frequency relation in log–log space. The black dashed line shows the best-fit line, and the red dashed lines show the uncertainty of the fit by randomly drawing from the joint posterior distribution of the slope (S) and intercept (I).

versus frequency relation and then use the Pearson correlation test[3] to estimate the correlation coefficient ρ and the probability (p-value) of a random correlation. We additionally fit a linear model ($y = S * x + I$) in log–log space. We repeat this process 10^3 times to create the posterior distribution for ρ, p-value, S, and I from which we estimate median and 68% confidence intervals. The results of the correlation coefficient, p-values, and best-fit line coefficients are given in Table A.2.

---

[3] The Pearson correlation test yields a correlation coefficient ρ defined between $[-1,1]$ where -1 denotes a perfect anti-correlation, 0 no correlation, and 1 a perfect correlation. The accompanying p-value is the random chance probability of such correlation. For any p-value > 0.05 the correlation is not considered statistically significant.

Following this procedure, we find that out of the 61 sources, only 17 (27.8%, 10 FSRQs and 7 BL Lacs) show a statistically significant trend of δ_{var} changing with frequency. We discuss our interpretation for the trends below. Based on the Pearson correlation p-values (P), we can estimate the false-positive rate, that is, the number of sources where a significant trend could have been falsely identified, as $(\sum_{i=1}^{N} P_i)/N$. We find our false-positive rate to be 18% (3/17 sources).

4. Origin of the Doppler factor trend

Through the analysis discussed above we can identify three different trends:
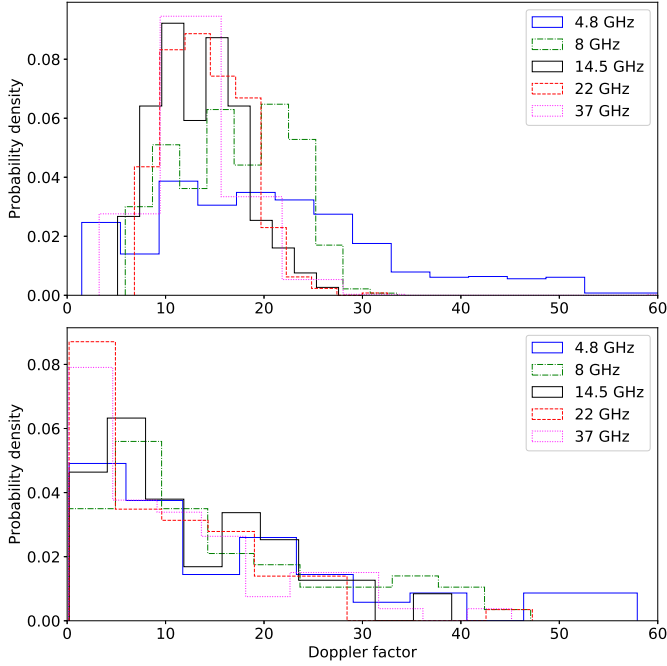
Fig. 2. *Top panel:* posterior Doppler factor distribution for 0716+714. *Bottom panel:* median Doppler factor distribution for all frequencies for the sources in our sample. For both panels, solid blue is for 4.8 GHz, dashed-dotted green for 8 GHz, solid black for 14.5 GHz, dashed red for 22 GHz, and dotted magenta for 37 GHz.

– No statistically significant trend. This is true for the majority of the sources in our sample (hereafter Sample A, 44 sources) suggesting no variation of the Doppler factor across frequencies.

– Doppler factor increases towards lower frequencies. This trend is found for 16 out of the 17 sources (hereafter Sample B) that show a statistically significant trend.

– Doppler factor increases towards higher frequencies. This trend is found for only one of the Sample B sources.

The fact that the majority of the sources in our sample do not show a statistically significant trend (Sample A) is consistent with the frequently used assumption of a straight conical jet with constant velocity. For the Sample B sources, the most common trend of an increasing δ_{var} towards lower frequencies was noted by Liodakis et al. (2017a) based on multiwavelength radio observations from the F-GAMMA program (Fuhrmann et al. 2016). Only 1253–055, also known as 3C 279, from Sample B shows the opposite trend, namely increasing δ_{var} towards higher frequencies. This trend is also confirmed by ALMA observations at 100 GHz (Fig. 5 panel c). The origin of the trends found in sample B can be attributed to either acceleration or jet bending. We discuss the possible interpretations below. For our comparisons, we use the Kolmogorov-Smirnov (K–S) test[4]. We also use the k-sample Anderson-Darling[5] (A–D) test to cross-check our results.
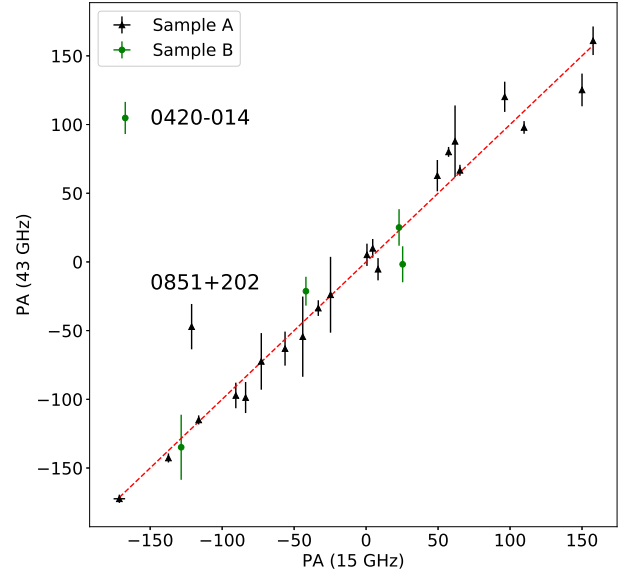

Fig. 3. Comparison of the innermost jet position angles at 15 and 43 GHz for Sample A (black) and Sample B (green). The red dashed line shows the 1–1 relation.

4.1. Changes in the viewing angle

To understand whether this trend is due to variations in the viewing angle produced by jet bending, we compare the innermost jet position angle (PA) at 15 GHz from the MOJAVE survey[6] (Pushkarev et al. 2012) and 43 GHz from the Boston University monitoring program[7] (Jorstad et al. 2017). Figure 3 shows that comparison for the common sources in Sample A (22 sources) and Sample B (5 sources). Only 0420–014 from Sample B shows a discrepancy in the jet PA suggesting the trend we find is due to a viewing angle change. A curved jet geometry for this source was previously noted by Britzen et al. (2000). The remaining four sources from Sample B, namely 0716+714, 0954+658, 1253–055, and 1749+096, show similar PA. Hence, the trend we detect in those sources, if real, is likely due to a velocity variation. Interestingly, 0851+202 (also known as OJ 287) in Sample A shows a slightly different PA between 15 and 43 GHz. However, the source is known to change its jet PA on timescales of 1–2 years (Cohen 2017; Britzen et al. 2018). Hence, this difference can be attributed to nonsimultaneous PA measurements at the two frequencies.

4.2. Transverse velocity structure

Recent observations of M87 revealed a transverse velocity structure (Mertens et al. 2016). A similar spine-sheath jet structure has been invoked to explain the discrepancy between δ_{var} implied by radio observations and spectral energy distribution modeling (e.g., Ghisellini et al. 2005). It is not unlikely that different frequencies not only probe different regions, but also a different underlying jet flow. In the standard spine-sheath model, where the spine is characterized by a faster flow, we would expect an increase of δ_{var} towards higher frequencies which is only observed in 1253–055. Mertens et al. (2016) found a more complex slow–fast–slow configuration in M 87. In this case, higher frequencies could be dominated by the innermost slower flow
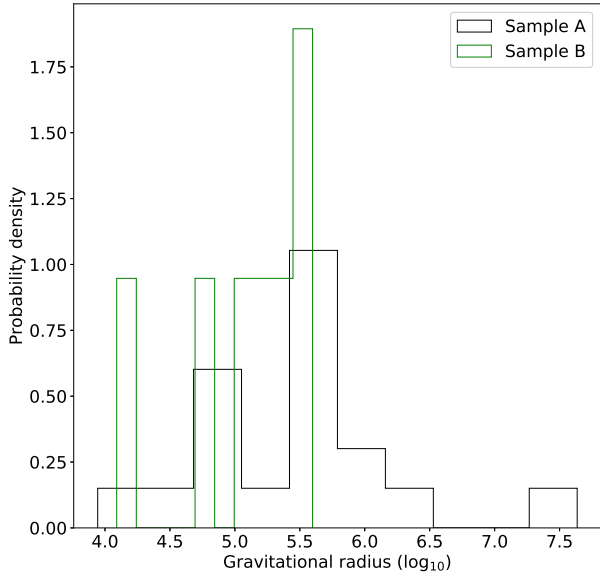

Fig. 4. Distance of the 15 GHz core from the black hole in gravitational radii for Sample A (black) and Sample B (green). We do not find a statistically significant difference between the two samples (K–S test p-value = 0.5).

with lower frequencies dominated by a faster flow, thus creating the observed trends.

4.3. Parabolic versus conical geometry

The shape of the jet can be studied using VLBI observations and by determining the width of the jet d as a function of distance r from the radio core. This is usually modeled with a power-law function $d \propto r^k$, where d can be estimated from a Gaussian fit to the transverse brightness profile with a FWHM D and the FWHM of the restoring beam b so that $d = (D^2 - b^2)^{1/2}$ (Pushkarev et al. 2017). In a conical jet, $k = 1$, while in a parabolic jet, $k = 0.5$. According to the jet-transition model, the acceleration zone in blazars is expected to end at $\sim 10^5$ gravitational radii (R_g, Marscher et al. 2008; Asada et al. 2014), where the jet is expected to change from parabolic to conical.

We estimate the distance from the black hole to the 15 GHz core in R_g using the de-projected core distance estimates from Pushkarev et al. (2012) and black hole masses from Liodakis & Petropoulou (2020). There are 18 sources in Sample A and 7 in Sample B with an available R_g estimate. Most of the sources cluster around $\sim 10^5 R_g$ (Fig. 4). One of the sources in Sample B has a distance $< 10^5 R_g$ (0212+735). Interestingly, 0212+735 also shows a geometry at 15 GHz closer to parabolic (k-index = 0.53). 0804+499 in Sample A shows a slightly lower value, although we do not detect a Doppler factor versus frequency trend. However, it is likely that the distance to the transition region ($\sim 10^5 R_g$) is not universal. The transition from a parabolic to a conical geometry can be different for different sources and occur closer to the black hole (Boccardi et al. 2016, 2021). Different VLBI studies can also produce discrepant results depending on the time-span used in the analysis (e.g., Boccardi et al. 2021; Park et al. 2021). Interestingly, Boccardi et al. (2021) find a parabolic geometry (k-index ≤ 0.6) for four sources common with our Sample A, namely 0316+413, 0430+052, 0415+379, and 1807+698 (3 radio galaxies and 1 BL Lac object), where we do not detect a significant trend. This
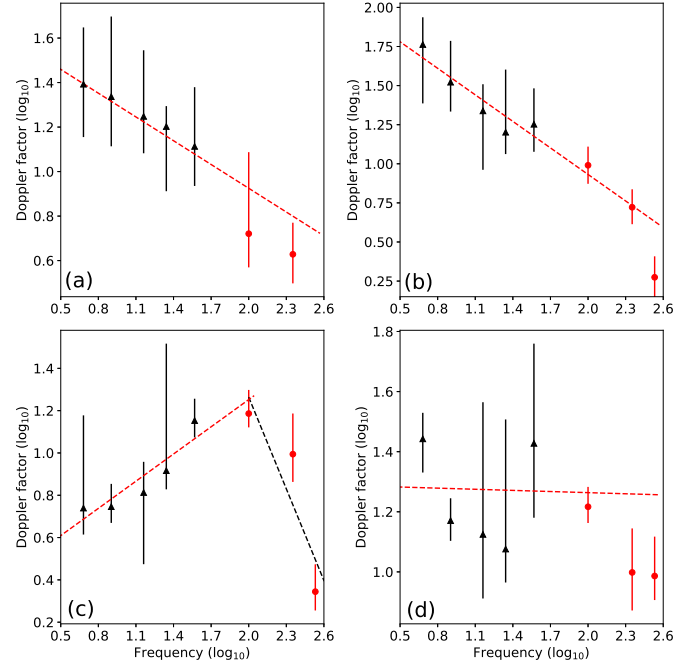

Fig. 5. Doppler factor versus frequency in log–log space for 0234+285 (*panel a*) 0420–014 (*panel b*), 1253–055 (*panel c*), and 2251+158 (*panel d*). The red dashed line shows the best-fit relation estimated in the 4.8–37 GHz range. The dashed black line in *panel c* is the best-fit relation estimated in the 100–350 GHz range.

discrepancy could be related to either the caveats discussed below (Sect. 4.5) or due to their low $\delta_{var} < 5$ preventing us from identifying any trend.

To further test the jet-transition scenario we turn to high-frequency (>37 GHz) observations. If the sources in Sample B are in the parabolic geometry regime, we expect the trend we find in the δ_{var} versus frequency plane to continue towards higher frequencies consistent with the best-fit trend. On the other hand, if the sources in Sample A are in the conical regime, towards higher frequencies we expect to find a transiting trend towards lower values for δ_{var}. We use data from the ALMA calibrator continuum observations catalog (Bonato et al. 2018)[8], CARMA at ~ 100 GHz (21 sources), and SMA (Gurwell et al. 2007)[9,10] at 225 GHz (45 sources) and 340 GHz (14 sources) to estimate δ_{var} following the same procedure as above (Sect. 2). There are a few additional sources from our sample included in those databases. However, those typically have less than 40 observations in total. We therefore excluded them from our analysis. The earliest ALMA and CARMA observation is at MJD 55701 (May 2011) and the latest is at MJD 59292 (March 2021). For the SMA observations, the earliest is at MJD 52431 (June 2006) while the latest is at MJD 59267 (February 2021). Table A.3 lists the high-frequency δ_{var} estimates.

Overall, we find that the high-frequency estimates for Sample A tend to be lower than the best-fit trend. From Sample B, 0716+714, 0736+017, and 1749+096 show lower δ_{var} similar to Sample A sources. On the other hand, 0234+285 and 0420–014 from Sample B show the expected behavior (Fig. 5 panels a, b). Given the difference in the innermost position angles found for

---

[8] https://almascience.eso.org/sc/
[9] http://sma1.sma.hawaii.edu/callist/callist.html
[10] The SMA observations for a given source are taken at slightly different frequencies (a dispersion of typically a few GHz). Here we quote the median frequency for all sources.

0420–014, this can therefore be interpreted as a continuously curved jet across the gigahertz range. Interestingly, 1253–055 shows a decreasing trend at high frequencies, although this is not statistically significant ($\rho = -0.88$ p-value = 0.3, Fig. 5 panel c). One interpretation could be that the jet is reaching terminal velocity close to 100 GHz and then decelerating. Recent Event Horizon telescope (EHT) observations at ∼230 GHz (Kim et al. 2020) found that the jet is likely bent. This could explain the change of trends from the high to low frequencies. Unlike 0420–014, the similar jet position angle between 43 and 15 GHz suggests that the trend of lower δ_{var} at lower frequencies is most likely due to deceleration. However, we note that the time window of the light curves used for the high-frequency modeling is shorter with little time overlap with the 4.8–37 GHz observations. Such a time difference can lead to underestimation of the δ_{var} at the highest frequencies. Although tantalizing, our results for the higher frequencies should be treated with caution.

Alternatively, acceleration at parsecs scales in a conical geometry can occur in a striped jet model with reversing toroidal magnetic field polarities (Zhang & Giannios 2021). In this case, jet acceleration is powered by magnetic energy dissipation via magnetic reconnection between stripes and can continue even after tens of parsecs from the black hole. This would suggest that Sample B sources likely host slower spinning supermassive black holes with a smaller stripe width spectral index (α). We test this scenario using the spin estimates from Liodakis (2018). There are 32 sources from Sample A and 12 sources from Sample B with an available estimate. We find no statistically significant difference between the two samples (K–S p-value = 0.97). We note that the spin estimates from Liodakis (2018) are model dependent and might not be representative of the "true" black hole spin of the sources.

4.4. Overall VLBI properties

Below, we additionally discuss the VLBI properties of the two samples using data from the MOJAVE survey (Kovalev et al. 2005; Pushkarev et al. 2012, 2017; Hovatta et al. 2014; Homan et al. 2015; Hodge et al. 2018; Lister et al. 2019). In the majority of cases, we do not find a statistically significant difference, and therefore we highlight just a few interesting comparisons.

We compare the median relative parallel and perpendicular acceleration (to their proper motion vector; see Eqs. (5) and (6) in Homan et al. 2015) of jet components in the two samples (28 sources from Sample A and 12 from Sample B). Parallel acceleration is often considered to reflect changes in the flow speed, while perpendicular acceleration is believed to reflect changes in the direction. Starting from the relative parallel acceleration, we do not find a statistically significant difference (K–S p-value = 0.33) between the two samples. If the measured acceleration of the jet components is representative of the jet bulk flow, one might expect Sample B sources to show higher acceleration. This would likely suggest that either Sample B is a mixture of accelerating sources and sources with changing viewing angles or that the acceleration of jet components reflects velocity changes of hotspots moving within an underlying, quiescent flow (e.g., Ghisellini & Tavecchio 2008). Interestingly, Sample B sources show on average higher relative perpendicular acceleration (K–S test p-value = 0.03). This would be in favor of either velocity stratification or jet bending producing the observed trends (see above).

Sample B sources are on average more core dominated (K–S p-value = 0.023, Kovalev et al. 2005). At the same time, the δ_{var}

distributions at 15 GHz do not show a significant difference (K–S test p-value = 0.56). This is in tension with the common assumption of the core dominance being a proxy for higher beaming, but our small sample size can also affect our conclusions. Sample A sources have on average higher maximum apparent jet velocity ($\beta_{\mathrm{app,max}}$, Lister et al. 2019). The K–S test rejects the null hypothesis when comparing the distributions for the two samples (p-value = 0.024) whereas the A–D test does not reject it, albeit marginally (p-value = 0.056). Excluding 1253–055 (which shows the opposite trend to the rest of the Sample B sources), both tests reject the null hypothesis (p-value < 0.026).

Using $\beta_{\mathrm{app,max}}$ and $\delta_{\mathrm{var,15}}$ we can estimate the viewing angle and Lorentz factor distributions. We do not find a significant difference in the viewing angle distributions (K–S p-value = 0.065). For the Lorentz factor distributions, the Sample B sources have on average lower values according to the K–S test (p-value = 0.02) which is not confirmed by the A–D test (p-value = 0.062). However, this trend is confirmed by both tests (p-value < 0.023) when excluding 1253–055. This could suggest that, on average, the remaining sources in Sample B (i.e., sources that show higher δ_{var} towards lower frequencies) have not yet reached Lorentz factors as high as those of Sample A sources at 15 GHz, that is, they are still accelerating.

4.5. Caveats

In the statistical analysis presented above, we used the available literature values. This often results in at least one sample (most often Sample B) having approximately or even fewer than ten sources, which hampers the discriminating strength of the K–S and A–D tests.

The cadence of the observations used for the light-curve modeling, if insufficient, can lead to an underestimation of the true Doppler factor in a given source (Liodakis & Pavlidou 2015b). Sources in our sample have varying average cadence, from a few days to a few weeks. Combined with the fact that flare rise times are expected to be shorter at higher frequencies, this can lead to the underestimation of the 22 and 37 GHz Doppler factors creating an artificial trend. Out of Sample B, 0458–020, 1739+522, 1803+784, 2007+777, and 2121+053 have a factor of two lower cadence at both high frequencies; hence the results from those sources should be treated with caution. The majority of our sources have comparable sampling, but it is nevertheless possible – although unlikely – that for some sources we are underestimating δ_{var} at the lower frequencies, and therefore destroying any intrinsic trend. If we are systematically underestimating the δ_{var} at 22 and 37 GHz, this would most likely suggest that the majority of our sources have decelerating jets or jets steering away from our line of sight.

Throughout this work, we assume the same value for the $T_{\mathrm{int,max}}$ for all frequencies. It could be possible for $T_{\mathrm{int,max}}$ to be different for different frequencies if for example the balance between particle and magnetic field energy densities changes with distance from the core. However, recent VLBI results at 86 GHz suggest a $T_{\mathrm{int,max}} \sim 3.7 \times 10^{11} K$ (Nair et al. 2019), consistent within the uncertainties from the 15 GHz value we used in this work. Hence, any $T_{\mathrm{int,max}}$ variations in the 4.8–37 GHz range are unlikely to have a significant impact on our results.

The δ_{var} estimates found in this work represent an average δ_{var} for a given observing period. Individual flares, can nevertheless yield both higher and lower δ_{var}. Changes in the viewing angle by factors of two to three during individual events have been noted in previous studies (e.g., Larionov et al. 2010; Raiteri et al. 2017; Uemura et al. 2017; Liodakis et al. 2020).

Variations in other geometric and physical parameters of the emission region (e.g., Lorentz factor, magnetic field strength etc.) are also possible. This is likely imprinted in the shape of the flares (Roy et al. 2019), which we find to have both symmetric and asymmetric (either fast rise–slow decay or slow rise–fast decay) profiles. The aforementioned δ_{var} variations are reflected in the estimates' accompanying confidence intervals (Tables A.1, A.3) which should not be treated as statistical, but instead as the possible range of δ_{var} for a given source.

5. Conclusions

We studied the relativistic effects across five radio frequencies from 4.8 to 37 GHz for 61 sources. By quantifying the Doppler factor in each frequency we are able to study variations possibly related to acceleration or deceleration, or jet bending. The majority of the sources in our sample do not show any such variations across frequencies. This would be consistent with nonaccelerating conical jets. However, we identify 17 interesting sources; 16 show higher Doppler factor towards lower frequencies and one shows the opposite trend. To test the different possible origins of δ_{var} versus frequency trends, we use the VLBI properties and high-frequency observations of the sources (100 GHz, 225 GHz, and 340 GHz; 45 sources have at least one high-frequency estimate) to estimate δ_{var} at such high frequencies for the first time. Our analysis suggests that the trend found in 0420–014 is likely due to jet bending, while the trend in 0212+735 is likely due to the jet accelerating in a parabolic geometry. 1253–055 shows a complex behavior that is likely attributed to a bend in the innermost jet probed by the highest frequencies, while decelerating at the 4.8–37 GHz range. For the remaining sources, our results are broadly consistent with the expectations from a transitioning geometry model with a few exceptions. However, the much shorter time-span of the high-frequency observations prevents us from coming to robust conclusions. Simultaneous high-cadence monitoring across the entire GHz–millimeter range – which will be available in the future with the Simons observatory (Ade et al. 2019) and CMB S4 (Abazajian et al. 2016) – will provide an unprecedented opportunity to study the structure of blazar jets through their multiwavelength radio variability.

References

Abazajian, K. N., Adshead, P., Ahmed, Z., et al. 2016, ArXiv e-prints [arXiv:1610.02743]
Ade, P., Aguirre, J., Ahmed, Z., et al. 2019, JCAP, 2019, 056
Aller, H. D., Aller, M. F., Latimer, G. E., & Hodge, P. E. 1985, ApJS, 59, 513
Aller, M. F., Aller, H. D., Hughes, P. A., & Latimer, G. E. 1999, ApJ, 512, 601
Aller, M. F., Hughes, P. A., Aller, H. D., Latimer, G. E., & Hovatta, T. 2014, ApJ, 791, 53
Angelakis, E., Fuhrmann, L., Nestoras, I., et al. 2010, ArXiv e-prints [arXiv:1006.5610]
Asada, K., & Nakamura, M. 2012, ApJ, 745, L28
Asada, K., Nakamura, M., Doi, A., Nagai, H., & Inoue, M. 2014, ApJ, 781, L2
Biretta, J. A., Sparks, W. B., & Macchetto, F. 1999, ApJ, 520, 621
Blandford, R. D., & Königl, A. 1979, ApJ, 232, 34
Blandford, R., Meier, D., & Readhead, A. 2019, ARA&A, 57, 467
Boccardi, B., Krichbaum, T. P., Bach, U., et al. 2016, A&A, 585, A33
Boccardi, B., Perucho, M., Casadio, C., et al. 2021, A&A, 647, A67
Bonato, M., Liuzzo, E., Giannetti, A., et al. 2018, MNRAS, 478, 1512
Brewer, B. J., & Foreman-Mackey, D. 2016, ArXiv e-prints [arXiv:1606.03757]
Brewer, B. J., Pártay, L. B., & Csányi, G. 2009, ArXiv e-prints [arXiv:0912.2380]
Britzen, S., Witzel, A., Krichbaum, T. P., et al. 2000, A&A, 360, 65
Britzen, S., Fendt, C., Witzel, G., et al. 2018, MNRAS, 478, 3199
Burd, P. R., Kohlhepp, L., Wagner, S. M., et al. 2021, A&A, 645, A62
Chatterjee, K., Liska, M., Tchekhovskoy, A., & Markoff, S. B. 2019, MNRAS, 490, 2200
Cohen, M. 2017, Galaxies, 5, 12
Fuhrmann, L., Angelakis, E., Zensus, J. A., et al. 2016, A&A, 596, A45
Georganopoulos, M., & Kazanas, D. 2003, ApJ, 594, L27
Ghisellini, G., & Tavecchio, F. 2008, MNRAS, 386, L28
Ghisellini, G., Tavecchio, F., & Chiaberge, M. 2005, A&A, 432, 401
Gurwell, M. A., Peck, A. B., Hostler, S. R., Darrah, M. R., & Katz, C. A. 2007, in From Z-Machines to ALMA: (Sub)Millimeter Spectroscopy of Galaxies, eds. A. J. Baker, J. Glenn, A. I. Harris, J. G. Mangum, & M. S. Yun, ASP Conf. Ser., 375, 234
Hodge, M. A., Lister, M. L., Aller, M. F., et al. 2018, ApJ, 862, 151
Homan, D. C., Kadler, M., Kellermann, K. I., et al. 2009, ApJ, 706, 1253
Homan, D. C., Lister, M. L., Kovalev, Y. Y., et al. 2015, ApJ, 798, 134
Hovatta, T., Valtaoja, E., Tornikoski, M., & Lähteenmäki, A. 2009, A&A, 494, 527
Hovatta, T., Aller, M. F., Aller, H. D., et al. 2014, AJ, 147, 143
Huppenkothen, D., Brewer, B. J., Hogg, D. W., et al. 2015, ApJ, 810, 66
Jorstad, S. G., Marscher, A. P., Morozova, D. A., et al. 2017, ApJ, 846, 98
Kharb, P., Lister, M. L., & Cooper, N. J. 2010, ApJ, 710, 764
Kim, J.-Y., Krichbaum, T. P., Broderick, A. E., et al. 2020, A&A, 640, A69
Komatsu, E., Dunkley, J., Nolta, M. R., et al. 2009, ApJS, 180, 330
Komissarov, S. S., Barkov, M. V., Vlahakis, N., & Königl, A. 2007, MNRAS, 380, 51
Kovalev, Y. Y., Kellermann, K. I., Lister, M. L., et al. 2005, AJ, 130, 2473
Kovalev, Y. Y., Pushkarev, A. B., Nokhrina, E. E., et al. 2020, MNRAS, 495, 3576
Larionov, V. M., Villata, M., & Raiteri, C. M. 2010, A&A, 510, A93
Liodakis, I. 2018, A&A, 616, A93
Liodakis, I., & Pavlidou, V. 2015a, MNRAS, 451, 2434
Liodakis, I., & Pavlidou, V. 2015b, MNRAS, 454, 1767
Liodakis, I., & Petropoulou, M. 2020, ApJ, 893, L20
Liodakis, I., Marchili, N., Angelakis, E., et al. 2017a, MNRAS, 466, 4625
Liodakis, I., Pavlidou, V., & Angelakis, E. 2017b, MNRAS, 465, 180
Liodakis, I., Pavlidou, V., Hovatta, T., et al. 2017c, MNRAS, 467, 4565
Liodakis, I., Hovatta, T., Huppenkothen, D., et al. 2018, ApJ, 866, 137
Liodakis, I., Blinov, D., Jorstad, S. G., et al. 2020, ApJ, 902, 61
Lister, M. L., Aller, M. F., Aller, H. D., et al. 2018, ApJS, 234, 12
Lister, M. L., Homan, D. C., Hovatta, T., et al. 2019, ApJ, 874, 43
Lyubarsky, Y. 2009, ApJ, 698, 1570
Lyubarsky, Y. E. 2010, MNRAS, 402, 353
Marscher, A. P. 1995, Proc. Nat. Acad. Sci., 92, 11439
Marscher, A. P., Jorstad, S. G., D'Arcangelo, F. D., et al. 2008, Nature, 452, 966
Mertens, F., Lobanov, A. P., Walker, R. C., & Hardee, P. E. 2016, A&A, 595, A54
Nair, D. G., Lobanov, A. P., Krichbaum, T. P., et al. 2019, A&A, 622, A92
Nokhrina, E. E., Kovalev, Y. Y., & Pushkarev, A. B. 2020, MNRAS, 498, 2532
Park, J., Hada, K., Nakamura, M., et al. 2021, ApJ, 909, 76
Piner, B. G., & Edwards, P. G. 2018, in Fourteenth Marcel Grossmann Meeting - MG14, eds. M. Bianchi, R. T. Jansen, & R. Ruffini, 3074
Potter, W. J., & Cotter, G. 2015, MNRAS, 453, 4070
Pushkarev, A. B., Hovatta, T., Kovalev, Y. Y., et al. 2012, A&A, 545, A113
Pushkarev, A. B., Kovalev, Y. Y., Lister, M. L., & Savolainen, T. 2017, MNRAS, 468, 4992
Raiteri, C. M., Villata, M., Acosta-Pulido, J. A., et al. 2017, Nature, 552, 374
Richards, J. L., Hovatta, T., Max-Moerbeck, W., et al. 2014, MNRAS, 438, 3058

Roy, N., Chatterjee, R., Joshi, M., & Ghosh, A. 2019, MNRAS, 482, 743

Salonen, E., Terasranta, H., Urpo, S., et al. 1987, A&AS, 70, 409

Savolainen, T., Wiik, K., Valtaoja, E., Jorstad, S. G., & Marscher, A. P. 2002, A&A, 394, 851

Sobolewska, M. A., Siemiginowska, A., Kelly, B. C., & Nalewajko, K. 2014, ApJ, 786, 143

Spruit, H. C., Foglizzo, T., & Stehle, R. 1997, MNRAS, 288, 333

Teräsranta, H., Tornikoski, M., Valtaoja, E., et al. 1992, A&AS, 94, 121

Teräsranta, H., Tornikoski, M., Mujunen, A., et al. 1998, A&AS, 132, 305

Teräsranta, H., Achren, J., Hanski, M., et al. 2004, A&A, 427, 769

Teräsranta, H., Wiren, S., Koivisto, P., Saarinen, V., & Hovatta, T. 2005, A&A, 440, 409

Uemura, M., Itoh, R., Liodakis, I., et al. 2017, PASJ, 69, 96

Vlahakis, N. 2004, Ap&SS, 293, 67

Vlahakis, N., & Königl, A. 2003, ApJ, 596, 1104

Vlahakis, N., & Königl, A. 2004, ApJ, 605, 656

Zhang, H., & Giannios, D. 2021, MNRAS, 502, 1145

Appendix A: Tables.

Table A.1. Median Doppler factor estimates and their 68% confidence intervals for all the sources in our sample. Column (1) is the B1950 name, column (2) is the redshift, column (3) is δ_{var} at 4.8 GHz, column (4) is δ_{var} at 8 GHz, column (5) is δ_{var} at 14.5 GHz, column (6) is δ_{var} at 22 GHz, and column (7) is δ_{var} at 37 GHz.

Name	z	$\delta_{var,4.8}$	$\delta_{var,8}$	$\delta_{var,14.5}$	$\delta_{var,22}$	$\delta_{var,37}$
0048-097	0.635	$13.33^{+11.79}_{-10.67}$	$14.34^{+12.36}_{-6.64}$	$8.35^{+7.71}_{-4.37}$	$4.04^{+1.79}_{-1.84}$	-
0059+581	0.644	$49.18^{+8.94}_{-10.91}$	$29.65^{+8.85}_{-10.34}$	$23.05^{+11.13}_{-8.44}$	$12.69^{+5.76}_{-3.68}$	$8.34^{+4.77}_{-2.24}$
0106+013	2.107	$20.06^{+30.99}_{-7.73}$	$22.46^{+16.94}_{-13.14}$	$19.22^{+8.86}_{-5.14}$	$14.59^{+5.91}_{-7.96}$	$13.36^{+3.71}_{-6.81}$
0109+224	0.265	$4.55^{+3.17}_{-0.99}$	$6.24^{+1.62}_{-1.63}$	$5.51^{+1.8}_{-1.39}$	$4.73^{+1.77}_{-1.52}$	$5.5^{+1.46}_{-1.52}$
0133+476	0.859	$29.71^{+12.8}_{-6.87}$	$9.14^{+17.61}_{-7.14}$	$16.47^{+6.07}_{-14.31}$	$16.96^{+3.75}_{-3.27}$	$18.99^{+4.33}_{-5.18}$
0202+149	0.834	$14.9^{+10.38}_{-7.0}$	$5.36^{+5.18}_{-2.91}$	$12.19^{+9.56}_{-6.39}$	$6.99^{+5.98}_{-2.71}$	$8.45^{+1.86}_{-2.41}$
0212+735	2.367	-	$40.95^{+18.72}_{-9.64}$	$25.73^{+12.51}_{-7.37}$	$22.78^{+7.01}_{-9.46}$	$10.81^{+4.26}_{-4.01}$
0234+285	1.213	$24.7^{+14.51}_{-13.51}$	$21.71^{+18.0}_{-11.15}$	$17.7^{+12.11}_{-6.76}$	$15.94^{+3.36}_{-10.68}$	$12.98^{+7.95}_{-5.31}$
0235+164	0.94	$53.71^{+15.63}_{-30.67}$	$34.77^{+22.9}_{-16.79}$	$26.46^{+10.2}_{-14.77}$	$27.24^{+6.73}_{-6.43}$	$27.54^{+18.6}_{-16.21}$
0300+470	0.475	$8.91^{+9.95}_{-7.16}$	$4.41^{+7.86}_{-1.57}$	$7.84^{+5.16}_{-2.23}$	$2.24^{+1.74}_{-1.71}$	$1.71^{+1.18}_{-0.86}$
0306+102	0.863	$8.23^{+2.17}_{-4.54}$	$7.69^{+3.89}_{-2.11}$	$9.54^{+1.45}_{-2.73}$	$4.37^{+1.51}_{-1.69}$	$2.75^{+1.79}_{-1.51}$
0316+413	0.018	$0.2^{+0.06}_{-0.05}$	$0.22^{+0.08}_{-0.06}$	$0.19^{+0.37}_{-0.07}$	$0.2^{+1.67}_{-0.09}$	$0.13^{+1.5}_{-0.03}$
0336-019	0.852	$22.82^{+6.46}_{-10.01}$	$16.28^{+4.06}_{-3.08}$	$18.99^{+5.97}_{-3.86}$	$7.85^{+3.19}_{-2.73}$	$13.79^{+7.23}_{-4.82}$
0415+379	0.048	$1.92^{+0.69}_{-0.21}$	$2.94^{+0.71}_{-1.39}$	$2.46^{+3.55}_{-1.24}$	$2.36^{+0.5}_{-0.46}$	$3.48^{+0.83}_{-0.85}$
0420-014	0.915	$57.92^{+23.21}_{-50.24}$	$33.26^{+20.22}_{-14.39}$	$21.8^{+8.54}_{-18.92}$	$15.92^{+14.68}_{-5.12}$	$17.9^{+9.46}_{-7.26}$
0422+004	0.268	$7.25^{+4.92}_{-5.77}$	$6.98^{+3.72}_{-2.52}$	$5.14^{+4.26}_{-1.66}$	$4.04^{+1.02}_{-1.01}$	$3.79^{+1.42}_{-1.25}$
0430+052	0.033	$2.82^{+2.07}_{-0.63}$	$1.81^{+1.98}_{-0.58}$	$2.59^{+0.83}_{-1.58}$	$2.8^{+0.78}_{-0.55}$	$2.48^{+0.77}_{-1.21}$
0458-020	2.291	$37.66^{+32.61}_{-24.62}$	$12.66^{+17.6}_{-7.13}$	$8.52^{+15.31}_{-1.3}$	$4.57^{+11.32}_{-3.19}$	$3.36^{+3.95}_{-2.43}$
0528+134	2.07	$39.98^{+15.75}_{-24.35}$	$40.23^{+20.68}_{-34.92}$	$35.92^{+31.81}_{-20.32}$	$47.26^{+33.51}_{-26.47}$	$28.01^{+21.12}_{-22.53}$
0605-085	0.872	$2.53^{+0.3}_{-0.18}$	$6.65^{+3.17}_{-3.45}$	$2.71^{+4.97}_{-0.35}$	$2.06^{+1.5}_{-1.01}$	$2.89^{+2.19}_{-2.21}$
0716+714	0.31	$19.94^{+11.99}_{-9.87}$	$16.71^{+6.51}_{-6.93}$	$13.64^{+4.46}_{-4.07}$	$13.83^{+4.55}_{-4.07}$	$12.41^{+5.4}_{-3.08}$
0735+178	0.424	$2.39^{+8.01}_{-1.59}$	$6.18^{+6.13}_{-3.27}$	$5.93^{+8.82}_{-1.68}$	$5.31^{+4.46}_{-1.8}$	$3.93^{+4.55}_{-2.14}$
0736+017	0.191	$7.61^{+2.34}_{-2.19}$	$7.8^{+2.99}_{-2.06}$	$6.19^{+2.8}_{-1.99}$	$5.57^{+1.22}_{-1.44}$	$5.63^{+1.37}_{-1.42}$
0754+100	0.266	$4.47^{+1.57}_{-1.19}$	$7.43^{+1.04}_{-1.62}$	$4.8^{+3.11}_{-1.54}$	$4.84^{+1.9}_{-2.16}$	$3.06^{+0.89}_{-1.14}$
0804+499	1.436	$36.61^{+17.73}_{-5.87}$	$12.55^{+14.92}_{-5.05}$	$30.49^{+12.93}_{-11.48}$	$28.4^{+8.18}_{-8.66}$	$30.84^{+7.87}_{-14.29}$
0814+425	1.381	$19.34^{+10.08}_{-6.19}$	$31.02^{+25.09}_{-22.33}$	$9.43^{+4.3}_{-3.4}$	$13.57^{+5.5}_{-8.8}$	$7.05^{+1.79}_{-2.54}$
0851+202	0.306	$15.17^{+9.57}_{-5.38}$	$25.16^{+8.26}_{-9.41}$	$17.04^{+7.37}_{-7.87}$	$19.46^{+15.42}_{-4.64}$	$27.97^{+13.29}_{-10.45}$
0954+658	0.367	$21.61^{+7.5}_{-10.87}$	$14.17^{+3.53}_{-3.47}$	$6.65^{+4.42}_{-1.72}$	$4.46^{+1.18}_{-2.05}$	$5.87^{+3.57}_{-1.92}$
1055+018	0.888	$12.78^{+11.28}_{-7.57}$	$12.75^{+6.59}_{-9.83}$	$9.49^{+17.25}_{-5.09}$	$15.4^{+5.54}_{-3.33}$	$18.05^{+7.58}_{-9.18}$
1101+3828	0.03	$3.33^{+1.01}_{-0.85}$	$3.19^{+0.74}_{-0.92}$	$2.25^{+0.5}_{-0.73}$	$2.81^{+0.53}_{-1.0}$	$2.55^{+1.44}_{-1.39}$
1156+295	0.729	$19.04^{+8.94}_{-15.03}$	$32.82^{+13.04}_{-22.63}$	$22.09^{+5.97}_{-15.58}$	$15.62^{+4.83}_{-3.6}$	$33.32^{+18.88}_{-20.58}$
1219+285	0.102	$0.86^{+0.6}_{-0.12}$	$0.6^{+1.52}_{-0.1}$	$1.45^{+0.81}_{-0.63}$	$0.47^{+0.9}_{-0.27}$	$0.47^{+1.24}_{-0.36}$
1222+216	0.435	$6.7^{+3.0}_{-3.42}$	$3.48^{+8.36}_{-2.83}$	$4.13^{+3.4}_{-2.81}$	$3.31^{+5.91}_{-1.31}$	$3.43^{+2.55}_{-0.87}$
1226+023	0.158	$4.27^{+2.43}_{-3.12}$	$5.71^{+4.34}_{-4.22}$	$4.43^{+1.04}_{-0.85}$	$6.0^{+2.37}_{-1.16}$	$4.25^{+3.09}_{-1.26}$
1253-055	0.536	$5.49^{+5.54}_{-1.58}$	$5.57^{+1.38}_{-0.99}$	$6.5^{+2.17}_{-1.68}$	$8.25^{+11.4}_{-1.68}$	$14.23^{+3.38}_{-2.61}$
1308+326	0.997	$10.4^{+10.89}_{-8.21}$	$13.38^{+14.23}_{-7.86}$	$9.19^{+3.87}_{-5.63}$	$13.94^{+7.87}_{-4.09}$	$13.87^{+7.11}_{-3.72}$
1335-127	0.539	$9.57^{+8.34}_{-2.14}$	$13.27^{+10.27}_{-5.37}$	$10.29^{+4.03}_{-3.47}$	$6.62^{+10.86}_{-2.45}$	$5.95^{+4.49}_{-1.47}$
1413+135	0.247	$4.05^{+2.49}_{-2.34}$	$5.36^{+8.56}_{-1.83}$	$7.41^{+2.62}_{-4.05}$	$4.67^{+1.64}_{-2.26}$	$2.63^{+0.95}_{-0.69}$
1418+546	0.152	$7.77^{+5.57}_{-5.55}$	$5.9^{+1.66}_{-1.77}$	$3.72^{+0.76}_{-2.34}$	$2.78^{+1.33}_{-0.9}$	$2.55^{+1.38}_{-2.32}$
1502+106	1.839	$9.97^{+9.59}_{-8.58}$	$25.87^{+26.44}_{-11.26}$	$31.21^{+13.37}_{-10.2}$	$10.02^{+6.4}_{-4.58}$	$12.27^{+8.19}_{-4.08}$
1510-089	0.36	$24.7^{+9.76}_{-7.77}$	$23.04^{+11.43}_{-10.97}$	$22.94^{+10.5}_{-11.91}$	$20.58^{+7.76}_{-5.67}$	$24.02^{+6.46}_{-11.13}$
1553+113	0.36	$1.56^{+3.57}_{-1.49}$	$0.34^{+2.68}_{-0.26}$	$0.68^{+3.68}_{-0.47}$	$1.13^{+1.05}_{-0.44}$	-
1611+343	1.397	$4.64^{+2.37}_{-1.42}$	$9.25^{+8.47}_{-6.41}$	$11.12^{+12.87}_{-7.59}$	$7.4^{+5.55}_{-4.51}$	$9.54^{+9.47}_{-5.72}$
1633+382	1.814	$29.02^{+28.37}_{-12.2}$	$37.89^{+15.03}_{-14.1}$	$39.07^{+10.16}_{-13.49}$	$24.99^{+15.97}_{-10.22}$	$45.15^{+23.92}_{-13.98}$
1641+399	0.593	$6.13^{+23.99}_{-1.61}$	$5.93^{+1.19}_{-2.65}$	$3.23^{+5.54}_{-1.05}$	$4.58^{+1.61}_{-0.84}$	$7.58^{+3.79}_{-3.67}$
1642+690	0.751	$5.24^{+4.94}_{-1.76}$	$10.15^{+3.53}_{-4.41}$	$4.57^{+2.71}_{-2.24}$	$3.58^{+2.87}_{-2.15}$	$3.78^{+3.26}_{-2.57}$
1730-130	0.902	$55.67^{+21.55}_{-24.35}$	$12.22^{+22.06}_{-2.04}$	$9.7^{+13.02}_{-4.79}$	$4.43^{+4.58}_{-1.75}$	$9.5^{+4.71}_{-4.38}$

Table A.1. continued.

Name	z	$\delta_{var,4.8}$	$\delta_{var,8}$	$\delta_{var,14.5}$	$\delta_{var,22}$	$\delta_{var,37}$
1739+522	1.379	$51.9^{+16.1}_{-13.21}$	$24.68^{+13.6}_{-9.64}$	$27.13^{+10.51}_{-8.27}$	$12.95^{+5.87}_{-2.5}$	$8.28^{+2.46}_{-3.29}$
1741-038	1.057	$20.21^{+22.15}_{-7.72}$	$18.46^{+13.75}_{-8.35}$	$22.76^{+21.51}_{-15.15}$	$15.38^{+9.33}_{-4.32}$	$23.11^{+7.74}_{-8.29}$
1749+096	0.322	$19.65^{+13.72}_{-8.73}$	$18.75^{+4.57}_{-5.16}$	$17.06^{+6.67}_{-6.07}$	$17.22^{+7.06}_{-7.11}$	$13.98^{+6.16}_{-2.29}$
1803+784	0.68	$26.94^{+10.86}_{-10.39}$	$19.35^{+15.23}_{-9.68}$	$19.24^{+5.59}_{-6.0}$	$6.81^{+2.54}_{-1.77}$	$8.33^{+2.08}_{-2.04}$
1807+698	0.051	$2.34^{+0.73}_{-0.69}$	$4.2^{+2.09}_{-2.94}$	$1.08^{+0.93}_{-0.81}$	$1.21^{+0.47}_{-0.46}$	$0.87^{+0.34}_{-0.21}$
1823+568	0.664	$8.23^{+6.33}_{-4.8}$	$9.4^{+10.13}_{-6.87}$	$5.23^{+3.07}_{-2.57}$	$2.88^{+1.79}_{-1.96}$	$3.67^{+1.86}_{-1.82}$
2005+403	1.736	$21.66^{+7.94}_{-6.97}$	$34.51^{+22.24}_{-11.45}$	$14.8^{+18.52}_{-14.01}$	$21.08^{+6.56}_{-7.71}$	$12.75^{+8.01}_{-11.35}$
2007+777	0.342	$12.39^{+3.47}_{-3.9}$	$13.57^{+7.32}_{-4.34}$	$6.22^{+6.02}_{-3.14}$	$4.23^{+1.41}_{-1.34}$	$2.94^{+1.48}_{-1.18}$
2121+053	1.941	$48.04^{+15.49}_{-18.62}$	$47.09^{+20.05}_{-10.58}$	$27.75^{+16.61}_{-14.94}$	$11.34^{+6.01}_{-4.11}$	$14.32^{+5.46}_{-6.25}$
2200+420	0.069	$8.43^{+6.46}_{-6.68}$	$9.75^{+3.43}_{-3.34}$	$7.93^{+3.91}_{-3.58}$	$7.34^{+3.51}_{-1.93}$	$9.95^{+5.06}_{-4.39}$
2223-052	1.404	$10.08^{+29.59}_{-5.47}$	$37.38^{+50.69}_{-24.05}$	$21.0^{+20.54}_{-15.18}$	$13.38^{+6.12}_{-6.08}$	$21.68^{+7.95}_{-8.11}$
2230+114	1.037	$31.82^{+26.39}_{-25.91}$	$23.45^{+14.49}_{-13.6}$	$18.41^{+28.4}_{-10.33}$	$26.51^{+11.7}_{-9.55}$	$22.65^{+11.11}_{-10.21}$
2251+158	0.859	$27.72^{+5.53}_{-7.15}$	$14.82^{+2.53}_{-2.3}$	$13.33^{+13.5}_{-6.55}$	$11.91^{+11.83}_{-3.05}$	$26.78^{+20.46}_{-15.26}$
2254+074	0.19	$2.14^{+2.22}_{-1.06}$	$2.65^{+1.54}_{-1.27}$	$1.52^{+0.46}_{-0.29}$	$1.52^{+0.96}_{-1.08}$	$1.11^{+0.58}_{-0.6}$

Table A.2. Doppler factor versus frequency correlation results. Column (1) is the B1950 name, column (2) is the median Pearson correlation ρ, column (3) is the median Pearson correlation p-value, column (4) is the median best-fit slope, column (5) is the median best-fit intercept, and column (6) is the sample designation. "A" is for sources that do not show a statistically significant trend, "B" is for sources that do.

Name	ρ	p-value	slope	intercept	Sample
0048-097	-0.9	0.0998	$-0.85^{+0.66}_{-0.48}$	$1.84^{+0.49}_{-0.75}$	A
0059+581	-0.99	0.0014	$-0.83^{+0.21}_{-0.19}$	$2.25^{+0.2}_{-0.24}$	B
0106+013	-0.88	0.0504	$-0.38^{+0.36}_{-0.39}$	$1.68^{+0.48}_{-0.46}$	A
0109+224	0.14	0.8271	$-0.03^{+0.19}_{-0.22}$	$0.76^{+0.26}_{-0.24}$	A
0133+476	-0.11	0.8654	$-0.17^{+0.26}_{-0.23}$	$1.44^{+0.29}_{-0.38}$	A
0202+149	-0.31	0.6098	$-0.17^{+0.34}_{-0.3}$	$1.15^{+0.38}_{-0.45}$	A
0212+735	-0.97	0.0313	$-0.87^{+0.3}_{-0.36}$	$2.44^{+0.43}_{-0.38}$	B
0234+285	-1.0	0.0002	$-0.36^{+0.38}_{-0.31}$	$1.64^{+0.37}_{-0.44}$	B
0235+164	-0.85	0.0664	$-0.27^{+0.36}_{-0.32}$	$1.8^{+0.37}_{-0.46}$	A
0300+470	-0.83	0.0809	$-0.87^{+0.48}_{-0.42}$	$1.63^{+0.53}_{-0.55}$	A
0306+102	-0.81	0.0951	$-0.5^{+0.31}_{-0.32}$	$1.33^{+0.32}_{-0.39}$	A
0316+413	-0.77	0.1303	$0.48^{+0.61}_{-0.6}$	$-1.07^{+0.55}_{-0.53}$	A
0336-019	-0.65	0.2305	$-0.3^{+0.25}_{-0.24}$	$1.53^{+0.25}_{-0.31}$	A
0415+379	0.67	0.2114	$0.19^{+0.17}_{-0.17}$	$0.22^{+0.2}_{-0.23}$	A
0420-014	-0.93	0.0213	$-0.57^{+0.37}_{-0.29}$	$2.06^{+0.32}_{-0.47}$	B
0422+004	-0.97	0.0058	$-0.36^{+0.37}_{-0.28}$	$1.15^{+0.33}_{-0.51}$	B
0430+052	0.16	0.7962	$-0.08^{+0.26}_{-0.29}$	$0.49^{+0.33}_{-0.33}$	A
0458-020	-0.98	0.0044	$-1.06^{+0.49}_{-0.49}$	$2.26^{+0.54}_{-0.58}$	B
0528+134	-0.46	0.4346	$-0.04^{+0.42}_{-0.44}$	$1.65^{+0.43}_{-0.56}$	A
0605-085	-0.32	0.5977	$-0.16^{+0.29}_{-0.36}$	$0.7^{+0.34}_{-0.3}$	A
0716+714	-0.96	0.0092	$-0.2^{+0.3}_{-0.24}$	$1.38^{+0.31}_{-0.42}$	B
0735+178	0.35	0.5591	$0.0^{+0.56}_{-0.52}$	$0.75^{+0.65}_{-0.73}$	A
0736+017	-0.92	0.0258	$-0.19^{+0.19}_{-0.17}$	$1.03^{+0.21}_{-0.23}$	B
0754+100	-0.59	0.2914	$-0.25^{+0.19}_{-0.25}$	$0.95^{+0.24}_{-0.22}$	A
0804+499	-0.84	0.0733	$-0.17^{+0.19}_{-0.26}$	$1.69^{+0.25}_{-0.21}$	A

Table A.2. continued.

Name	ρ	p-value	slope	intercept	Sample
0814+425	-0.79	0.1134	$-0.64^{+0.29}_{-0.26}$	$1.88^{+0.28}_{-0.4}$	A
0851+202	0.58	0.3099	$0.22^{+0.29}_{-0.29}$	$1.07^{+0.32}_{-0.35}$	A
0954+658	-0.91	0.0313	$-0.72^{+0.28}_{-0.25}$	$1.75^{+0.28}_{-0.33}$	B
1055+018	0.54	0.3491	$0.16^{+0.37}_{-0.35}$	$0.96^{+0.41}_{-0.5}$	A
1101+384	-0.68	0.2022	$-0.15^{+0.24}_{-0.34}$	$0.59^{+0.32}_{-0.28}$	A
1156+295	0.18	0.7758	$0.1^{+0.43}_{-0.36}$	$1.23^{+0.39}_{-0.57}$	A
1219+285	-0.44	0.4578	$-0.25^{+0.45}_{-0.45}$	$0.21^{+0.45}_{-0.45}$	A
1222+216	-0.75	0.1479	$-0.19^{+0.37}_{-0.36}$	$0.9^{+0.43}_{-0.52}$	A
1226+023	0.02	0.9727	$0.08^{+0.41}_{-0.31}$	$0.62^{+0.35}_{-0.53}$	A
1253-055	0.91	0.0322	$0.43^{+0.23}_{-0.27}$	$0.4^{+0.36}_{-0.27}$	B
1308+326	0.47	0.4237	$0.06^{+0.45}_{-0.35}$	$1.01^{+0.44}_{-0.6}$	A
1335-127	-0.78	0.1236	$-0.3^{+0.29}_{-0.3}$	$1.33^{+0.35}_{-0.33}$	A
1413+135	-0.38	0.5244	$-0.26^{+0.33}_{-0.3}$	$0.94^{+0.39}_{-0.41}$	A
1418+546	-0.98	0.0026	$-0.62^{+0.35}_{-0.4}$	$1.3^{+0.41}_{-0.44}$	B
1502+106	-0.12	0.8482	$-0.14^{+0.48}_{-0.37}$	$1.39^{+0.42}_{-0.62}$	A
1510-089	-0.38	0.528	$-0.08^{+0.25}_{-0.25}$	$1.44^{+0.28}_{-0.33}$	A
1553+113	-0.07	0.9331	$-0.2^{+0.82}_{-0.8}$	$0.35^{+0.85}_{-0.96}$	A
1611+343	0.59	0.2927	$0.26^{+0.36}_{-0.39}$	$0.66^{+0.4}_{-0.45}$	A
1633+382	0.33	0.5925	$0.04^{+0.34}_{-0.31}$	$1.49^{+0.37}_{-0.4}$	A
1641+399	0.04	0.9452	$-0.25^{+0.47}_{-0.47}$	$1.08^{+0.61}_{-0.6}$	A
1642+690	-0.65	0.2395	$-0.36^{+0.35}_{-0.43}$	$1.12^{+0.46}_{-0.4}$	A
1730-130	-0.78	0.1202	$-0.93^{+0.35}_{-0.34}$	$2.2^{+0.38}_{-0.41}$	A
1739+522	-0.95	0.0127	$-0.86^{+0.23}_{-0.24}$	$2.29^{+0.26}_{-0.29}$	B
1741-038	0.11	0.864	$-0.04^{+0.32}_{-0.33}$	$1.36^{+0.39}_{-0.43}$	A
1749+096	-0.93	0.0222	$-0.13^{+0.28}_{-0.28}$	$1.4^{+0.32}_{-0.37}$	B
1803+784	-0.88	0.0473	$-0.66^{+0.24}_{-0.23}$	$1.9^{+0.27}_{-0.32}$	B
1807+698	-0.8	0.1023	$-0.62^{+0.25}_{-0.22}$	$0.9^{+0.28}_{-0.33}$	A
1823+568	-0.87	0.0549	$-0.61^{+0.44}_{-0.41}$	$1.41^{+0.46}_{-0.54}$	A
2005+403	-0.65	0.2305	$-0.31^{+0.26}_{-0.37}$	$1.68^{+0.35}_{-0.35}$	A
2007+777	-0.96	0.0089	$-0.79^{+0.23}_{-0.28}$	$1.73^{+0.28}_{-0.29}$	B
2121+053	-0.91	0.0339	$-0.75^{+0.26}_{-0.27}$	$2.25^{+0.28}_{-0.32}$	B
2200+420	0.04	0.9439	$-0.01^{+0.41}_{-0.32}$	$0.96^{+0.35}_{-0.55}$	A
2223-052	0.17	0.7883	$-0.17^{+0.51}_{-0.46}$	$1.51^{+0.61}_{-0.67}$	A
2230+114	-0.47	0.4209	$-0.15^{+0.43}_{-0.35}$	$1.54^{+0.41}_{-0.55}$	A
2251+158	-0.13	0.8358	$-0.01^{+0.25}_{-0.3}$	$1.29^{+0.28}_{-0.25}$	A
2254+074	-0.88	0.0471	$-0.43^{+0.37}_{-0.41}$	$0.74^{+0.45}_{-0.48}$	B

Table A.3. High-frequency Doppler factor estimates for the sources in our sample. Column (1) is the B1950 name, column (2) is δ_{var} at 100 GHz, column (3) is δ_{var} at 225 GHz, column (4) is δ_{var} at 340 GHz.

Name	$\delta_{var,100}$	$\delta_{var,225}$	$\delta_{var,340}$
0048-097	-	$0.47^{+0.2}_{-0.13}$	-
0059+581	-	$4.11^{+1.27}_{-0.69}$	-
0133+476	-	$3.78^{+0.72}_{-0.82}$	-
0234+285	$5.26^{+4.44}_{-1.83}$	$4.25^{+1.39}_{-1.28}$	-
0235+164	$6.84^{+2.81}_{-2.43}$	$5.96^{+1.28}_{-1.41}$	$2.23^{+0.61}_{-0.54}$
0300+470	-	$1.36^{+0.62}_{-0.39}$	-
0306+102	-	$1.97^{+0.78}_{-0.54}$	-
0316+413	$0.59^{+0.25}_{-0.28}$	$0.28^{+0.14}_{-0.12}$	$0.08^{+0.05}_{-0.06}$
0336-019	-	$2.6^{+0.55}_{-0.4}$	-
0415+379	-	$1.57^{+0.26}_{-0.29}$	$0.29^{+0.08}_{-0.09}$
0420-014	$9.78^{+2.69}_{-2.67}$	$5.27^{+1.4}_{-1.31}$	$1.88^{+0.58}_{-0.61}$
0430+052	-	$0.51^{+0.11}_{-0.1}$	-
0458-020	-	$3.22^{+1.69}_{-1.34}$	-
0528+134	-	$7.82^{+2.73}_{-2.28}$	$3.5^{+1.4}_{-0.9}$
0605-085	-	$1.68^{+1.13}_{-0.77}$	-
0716+714	$2.44^{+1.05}_{-1.12}$	$2.01^{+0.52}_{-0.7}$	-
0736+017	$2.53^{+0.35}_{-0.36}$	$0.95^{+0.22}_{-0.18}$	-
0814+425	-	$0.79^{+0.58}_{-0.22}$	-
0851+202	$5.65^{+1.02}_{-0.8}$	$3.16^{+0.61}_{-0.71}$	$1.68^{+0.37}_{-0.44}$
0954+658	-	$4.7^{+1.41}_{-1.45}$	-
1055+018	$6.67^{+0.94}_{-1.21}$	$5.35^{+1.17}_{-0.87}$	$1.37^{+1.29}_{-0.74}$
1101+384	$0.97^{+0.25}_{-0.46}$	-	-
1156+295	$7.15^{+2.55}_{-2.46}$	$3.35^{+0.95}_{-0.85}$	-
1222+216	$2.15^{+1.11}_{-1.05}$	$1.18^{+0.23}_{-0.26}$	-
1226+023	$3.35^{+0.68}_{-0.73}$	$5.47^{+2.21}_{-1.93}$	$2.13^{+0.55}_{-0.53}$
1253-055	$15.35^{+3.95}_{-2.31}$	$9.87^{+4.37}_{-2.98}$	$2.21^{+0.66}_{-0.45}$
1308+326	-	$2.3^{+0.59}_{-0.48}$	-
1335-127	$3.31^{+1.59}_{-1.2}$	$3.81^{+1.09}_{-0.9}$	-
1413+135	-	$0.51^{+0.17}_{-0.12}$	-
1418+546	-	$0.31^{+0.18}_{-0.16}$	-
1502+106	-	$3.32^{+1.03}_{-0.84}$	-
1510-089	$3.68^{+1.37}_{-0.83}$	$2.99^{+0.84}_{-0.68}$	-
1611+343	-	$1.54^{+0.8}_{-0.53}$	-
1633+382	-	$4.53^{+1.27}_{-0.61}$	-
1641+399	$4.94^{+1.57}_{-2.98}$	$4.23^{+0.71}_{-0.64}$	-
1642+690	-	$1.7^{+1.01}_{-0.93}$	-
1730-130	$8.47^{+2.07}_{-2.2}$	$5.24^{+2.56}_{-1.97}$	$2.13^{+0.8}_{-0.79}$
1741-038	-	$5.83^{+1.58}_{-1.27}$	$0.95^{+0.99}_{-0.41}$
1749+096	$5.53^{+1.38}_{-1.19}$	$3.65^{+1.15}_{-1.05}$	$1.01^{+0.24}_{-0.21}$
1803+784	-	$2.28^{+0.39}_{-0.3}$	-
1807+698	-	$0.25^{+0.11}_{-0.11}$	-
2121+053	-	$1.54^{+0.7}_{-0.4}$	-
2200+420	$1.89^{+0.49}_{-0.31}$	$1.84^{+0.58}_{-0.38}$	$0.66^{+0.22}_{-0.18}$
2223-052	-	$3.25^{+0.87}_{-0.69}$	-
2230+114	$10.59^{+2.96}_{-2.99}$	$7.52^{+1.4}_{-1.58}$	-
2251+158	$16.47^{+2.51}_{-2.05}$	$9.96^{+3.36}_{-2.9}$	$9.69^{+2.92}_{-1.79}$